Accepted Manuscript

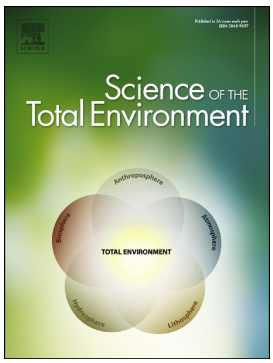

NanoRefinery of carbonaceous nanomaterials: Complementing dairy manure gasification and their applications in cellular imaging and heavy metal sensing

J. Plácido, S. Bustamante-López, K.E. Meissner, D.E. Kelly, S.L. Kelly

PII: S0048-9697(19)32963-8
DOI: https://doi.org/10.1016/j.scitotenv.2019.06.390
Reference: STOTEN 33044

To appear in: *Science of the Total Environment*

Received date: 12 April 2019
Revised date: 3 June 2019
Accepted date: 23 June 2019

Please cite this article as: J. Plácido, S. Bustamante-López, K.E. Meissner, et al., NanoRefinery of carbonaceous nanomaterials: Complementing dairy manure gasification and their applications in cellular imaging and heavy metal sensing, Science of the Total Environment, https://doi.org/10.1016/j.scitotenv.2019.06.390

NanoRefinery of carbonaceous nanomaterials: complementing dairy manure gasification and their applications in cellular imaging and heavy metal sensing

J. Plácido[*1], S. Bustamante-López[1, 2], K.E. Meissner[2], D.E. Kelly[1] and S.L. Kelly[1*]

1 Institute of Life Science (ILS 1), Swansea University Medical School, Swansea, Wales, UK, Swansea, SA2 8PP, Wales, UK

2 Department of Physics, Centre for NanoHealth, Swansea University, Swansea, SA2 8PP, Wales, UK

ABSTRACT

This article describes an efficient method, combining chemical oxidation and acetone extraction, to produce carbonaceous nanomaterials from dairy manure biochar. The optical and mechanical properties are similar to methods previously reported carbonaceous nanomaterials from biomass. Our novel process cuts the processing time in half and drastically reduces the energy input required. The acetone extraction produced 10 fractions with dairy manure biochar-derived carbonaceous nanomaterials (DMB–CNs). The fraction with the carbonaceous nanomaterials, DMB–CN-E1, with highest fluorescence was selected

[*] Corresponding authors:
Address: Institute of Life Science 1, Medical School, Swansea University, Swansea SA2 8PP, UK
Phone: +44 1792 503430 / +44 1792 662207
Fax: +44 1792 503430
Correspondance emails: j.e.placidoescobar@swansea.ac.uk / s.l.kelly@swansea.ac.uk

for in-depth characterisation and for initial testing across a range of applications. DMB–CN-E1 was characterised using atomic force microscope, electrophoresis, and spectrophotometric methods. DMB–CN-E1 exhibited a lateral dimension between 11 and 28 nm, a negative charge, and excitation/emission maxima at 337/410 nm, respectively. The bioimaging potential of DMB–CN-E1 evidenced different locations and different interactions with the cellular models evaluated. DMB–CN-E1 was quenched by several heavy metal ions showing a future application of these materials in heavy metal ion detection and/or removal. The demonstrated capabilities in bioimaging and environmental sensing create the opportunity for generating added-value nanomaterials (NanoRefinery) from dairy manure biochar gasification and, thus, increasing the economic viability of gasification plants.

Keywords: Carbonaceous nanomaterials; Dairy manure biochar; Chemical depolymerisation; Cell imaging; Heavy metal ions sensors; Gasification

1 INTRODUCTION

Worldwide, the cattle inventory is estimated to be around 1 billion head of cattle. This number of animals produces broad wastes including bedding material, feed wastes and manure. In fact, every day each animal produces, on average, approximately 8.2 kg of dry manure. With global cattle manure production around 3 billion tons per year (Nam et al., 2016), cattle are one of the largest waste producers in the agroindustry (Guo et al., 2010; Holm-Nielsen et al., 2009).

In light of this vast quantity, the focus of agro-industrial waste management has shifted from disposal to the reuse of these residues for the production of chemicals, energy, and/or

materials. Dairy manure has been successfully employed as a substrate for waste-to-energy production in anaerobic digestion (Burg et al., 2018; Ramírez-Arpide et al., 2018) and thermal conversion (Nam et al., 2016; Nam et al., 2017) processes. One of the thermal conversion processes is gasification. Gasification is a partial oxidation of a feedstock with the production of combustible gases (carbon monoxide and hydrogen) and residual biochar. These gases can be utilised for biofuel production via the Fisher-Tropsch process or for engine power generation. The biochar coproduced from bioenergy generation is used as soil amendment (Deal et al., 2012; Mukome et al., 2013; Wu et al., 2012) and activated carbons (Angın et al., 2013; Park et al., 2013).

The economic feasibility of a dairy manure gasification facility for power production was performed by Nam et al. 2016 (Nam et al., 2016). The authors made economic estimations based on a gasification system able to transform the daily manure production of 14.500 head of cattle from 4 farms in Texas, USA (118.9 tonnes of manure/day). This facility had a potential power generation of 2.5 MW with a £5.32 million net profit, at a minimum selling price of 0.061 £/kWh and a discounted payback period from 3.7 to 5 years (Nam et al., 2016). The study also assumed a biochar production equal to 5% of the original dairy manure and a price of 0.076 £/kg. Therefore, the potential gasification facility will produce approximately 6 tonnes of biochar daily and more than 2,000 tonnes of biochar every year. Similar to this facility, any type of gasification facility will produce excessive amounts of biochar, overwhelming storage capacity and current biochar derived products and applications. To improve the economic feasibility of thermal conversion facilities and overcome the emerging issues associated with biochar disposal and storage, it is necessary to develop novel biochar applications that can utilise the massive production of biochar from gasification facilities.

Biochar chemical depolymerisation, or oxidation, has been used as a method to transform biochar from bioenergy process into added-value products and to complement biomass thermal conversion. The chemical depolymerisation of cotton gin trash and municipal solid waste biochars produced added-value products, humic and fulvic acids as well as nanosilica (Genuino et al., 2017; Plácido and Capareda, 2015). In recent years, advanced materials have been produced from biochar using processes at high temperatures to transform different substrates such as pollen, spices and coffee beans (D'Angelis do ES et al., 2015; Essner et al., 2016; Vasimalai et al., 2018; Zhang et al., 2018). However, converting biomass into biochar with the sole aim of making advanced nanomaterials is a high energy cost process that misses the opportunity for bioenergy production. Moreover, biochar as a secondary product of bioenergy production is a co-product from the optimised conditions for syngas or bio-oil production. Thus, advanced materials derived from biochar under ideal conditions for nanomaterials production and from biochar by-product of bioenergy production have different characteristics and properties (D'Angelis do ES et al., 2015; Essner et al., 2016; Vasimalai et al., 2018; Zhang et al., 2018).

To date, biochar from dairy manure gasification, has not been evaluated for the production of advanced nanomaterials. Advanced nanomaterials have been produced using chemical and physical treatments from other types of biochar (Gao et al., 2017). Liou and Huang developed a two-step method to produce high graphene sheet content carbon materials from *Elaeis guineensis* and *Cryptomeria japonica* biochars. To produce 84% yield graphene materials, the biochars were pre-treated with acetic acid for 14 days followed by a 1500 °C heat treatment (Liou and Huang, 2015). Zhu et al. introduced the production of 3D graphene by incorporating hierarchical porous carbon. Their graphene material was produced by

carbonising (850 °C, 2 h, argon atmosphere) pre-treated *Auricularia* fungus which had absorbed graphite oxide molecules. The material produced had high conductivity, which allowed the material to be utilised as a supercapacitor (Zhu et al., 2015). Biochar has also been proposed as a viable option to produce Carbon dots (Cdots) using a combination of sulphuric and nitric acid as oxidising agents, and dialysis as the preferred separation method (Tour et al., 2016). Wang et al. transformed rice husk biochar into Cdots using a combination of oxidation, high temperatures and ultra-sonication (Wang et al., 2015). The Cdots from rice husk biochar exhibited bright and tuneable photoluminescence, biocompatibility and low cost. D'Angelis do E. S. Barbosa et al. described the production of Cdots from calcined cow manure at 300 °C using chemical oxidation with nitric acid for 72 h. In this case, the raw manure was used exclusively as a substrate for charcoal and Cdot production (D'Angelis do ES et al., 2015).

Biochar depolymerisation methods release carbonaceous compounds from the biochar into the liquid phase. Oxidising methods employed in biochar depolymerisation are similar to the methods employed for the production of carbonaceous nanomaterial from low and high rank coal as well as from other types of biochar (Tour et al., 2016). It is possible then, that carbonaceous nanomaterials can be produced from bioenergy-biochar depolymerisation. In this work, we explored carbonaceous nanomaterial production as an additional application to manage and extract additional value from the vast amounts of dairy manure biochar produced through bioenergy processes. The aim of this research was to evaluate the combination of chemical depolymerisation and solvent extraction as a rapid, low-cost method to produce carbonaceous nanomaterials from dairy manure biochar co-produced from bioenergy production. The best fraction of the dairy manure biochar–derived carbonaceous

nanomaterials (BCNs) was characterised, and its application to bio-imaging and heavy metal ions detection was investigated.

2 MATERIALS AND METHODS

2.1 Substrate

Dairy manure was used for bioenergy production. The dairy manure biochar (DMB) was kindly donated by Dr Sergio Capareda and his laboratory, the Bio-Energy Testing and Analysis Laboratory (BETA Lab) at Texas A&M University. DMB was produced from dairy manure in a fluidised bed/gasification process at 700 °C (Nam et al., 2016). After gasification, dairy manure biochar was collected from the reactor and sieved using a 1 mm mesh.

2.2 Chemicals

All chemicals were analytical grade: potassium permanganate ($KMnO_4$) (Alfa Aesar), acetone (Acros Organics), potato dextrose broth (PDB) medium (ForMedium), Roswell park memorial institute (RPMI) medium (Sigma–Aldrich), Murashige and Skoog (MS) medium (Sigma-Aldrich), PBS (Sigma–Aldrich). The heavy metal ions included: Nickel sulphate (Ni(II)) (Fisher Scientific), Copper sulphate (Cu (II)), Cadmium sulphate (Cd (II)), Lead Nitrate (Pb (II)), Cobalt nitrate (Co (II)) (Sigma–Aldrich), Barium chloride (Ba (II)) (Sigma–Aldrich), lithium acetate (Li (I)) (Sigma–Aldrich), iron sulphate (Fe(II)) (Sigma–Aldrich), manganese chloride (Mn (II)) (Acros Organics), zinc sulphate (Zn (II)) (Sigma–Aldrich), silver nitrate (Ag (I)) (Sigma–Aldrich), sodium molybdate (Mo (VI))

(Sigma–Aldrich). Deionised and filtered (Milli–Q ultrapure water system with a 0.22 µm filter, Merck Millipore) water was utilised in all the procedures.

2.3 Biochar chemical depolymerisation

The biochar depolymerisation reaction was as follows: 10 % solutions of $KMnO_4$ (as an oxidising agent) were mixed with DMB (5 %) in 125 mL Erlenmeyer flasks. The depolymerisation was performed at 120 °C for 1 h at 15 psi in an autoclave (Med 12, Selecta) following the protocol developed by Placido and Capareda (Plácido and Capareda, 2015). After the chemical depolymerisation, the biochar solutions were centrifuged at 5000 rpm for 20 min at room temperature to separate the liquid and solid phases. The liquid phase was filtered using 0.22 µm filters (Millex) and refrigerated at −20 °C until use. The depolymerised biochar was dried in a convection oven at 105 °C for 24 h. The initial DMB, water-treated DMB (biochar in aqueous solution without $KMnO_4$ and autoclave conditions) and a $KMnO_4$ solution without biochar were utilised as controls.

2.4 Purification of dairy manure biochar–derived carbonaceous nanomaterials

An initial acetone precipitation step (acetone extraction 1) was carried out in centrifuge tubes using the filtered biochar depolymerisation liquid phase. After acetone addition, the sample was agitated for 1 min using a vortexer. Acetone addition produced small brown/reddish aggregates throughout the volume of the solution. The small aggregates assembled until they formed a viscous colloidal suspension in the bottom of the sample. The first addition of acetone generated three phases a supernatant (supernatant 1), a brownish colloidal suspension (suspension 1), and a solid phase (pellet 1). To improve phase

separation, the samples were centrifuged at 5000 rpm for 20 min (Legend RT, Sorvall). The liquid phases (supernatant 1, suspension 1) were roto-evaporated (miVAc Quattro concentrator, Genevac) to completely remove the acetone/water mixture. The solid phase (pellet 1) was dried at 60 °C for 48 h. After weighing, the three fractions were resuspended in 5 ml of water and ultrasonicated for 1 min at 50 % amplitude (Branson, Emerson). Then, the acetone precipitation step was repeated for each of the resuspended phases (Acetone extraction 2). Supernatant 1 and colloidal suspension 1 each produced a supernatant and a colloidal suspension, without pellet production. Whereas, pellet 1 produced a solid and a supernatant. The 5 liquid phases were again roto-evaporated, resuspended and ultrasonicated as previously described. A final acetone precipitation step was performed for the 5 liquid fractions previously obtained (acetone extraction 3). Each fraction produced light and heavy phases reaching a total of 10 fractions. These fractions were roto-evaporated, resuspended and ultrasonicated. The fractions are described in **Table 1** and the extraction sequence is explained in the supplementary material**.** The fluorescence spectra (emission and excitation) of the different fractions were obtained on a Hitachi F2500 spectrophotometer. The fraction with the highest fluorescence was chosen for further characterisation. The recovery percentage was calculated as a proportion between the weights of each fraction and the original weight of the liquid phase after biochar oxidation.

2.5 Dairy manure biochar–carbonaceous nanomaterials characterisation

The liquid fraction with the highest fluorescence after the purification process was evaluated using spectrophotometry, atomic force microscopy (AFM), Fourier-transform infrared spectroscopy (FTIR) and Zetasizer size and charge measurements. The fluorescence emission and excitation spectra of the different fractions were obtained on a Hitachi F2500

spectrophotometer. FTIR spectra of the different fractions were collected using a Frontier FT–IR spectrophotometer with sampler (PerkinElmer) from 4000−600 cm^{-1}. UV–Vis absorption spectra were recorded using a U3310 spectrophotometer (Hitachi). Atomic force microscopy (AFM) images were captured on a BioScope AFM (Bruker Corporation.) in ScanAsyst® mode, a PeakForce Tapping® based image optimisation technique (tip radius nominally 2 nm and with a maximum of 12 nm) and the image analysis was performed using the Bruker NanoScope software package v8.15 (Bruker Corporation). The dairy manure biochar–carbonaceous nanomaterials (DMB–CN) size, zeta potential in solution were obtained by dynamic light–scattering (DLS) and laser doppler velocimetry (LDV) using the Zetasizer Nano ZS (Malvern). The measurement was performed using 0.2 µm filtered solutions in a DTS1070 cell, with water as dispersant (Refractive Index: 1.330) and DMB–CNs refractive index estimated as 2.418 (Nguyen et al., 2016). The pH effect on DMB–CNs was evaluated using fluorescence, UV–Vis and FT–IR spectroscopies. The DMB–CNs solution pH was reduced using hydrochloric acid (HCl) 1 M.

2.6 Biocompatibility studies

DMB–CN biocompatibility was studied in three yeast species: *Saccharomyces cerevisiae* AH22, *Candida albicans SC 5314, and Yarrowia lipolytica (*ATCC 46483*).* These species belong to the yeast collection of the cytochrome P450 group at Swansea University. The yeast growth curve studies were performed on a Bioscreen C instrument (Oy Growth Curves Ab Ltd). Five different DMB–CN concentrations (50, 100, 250, 500, 1000 ppm) were evaluated in wells with 200 µL of PDB and 100 µL of 1×10^5 cells mL^{-1} inoculum and 3 replicates for each concentration. The cell concentration change in each well was evaluated

via the optical density change at a wavelength of 600 nm for 72 h and 30 °C. The growth curves were also evaluated using DMB–CNs at pH 10, 7, and 3.

2.7 Cellular imaging

The potential applications of DMB–CNs as fluorescent probes for cellular bio-imaging were evaluated in three yeast species (*S. cerevisiae* AH22*, C. albicans SC 5314, and Y. lipolytica (*ATCC 46483*),* human TK6 cells and plant cells from *Nicotiana tabacum*. Yeast species were cultured in PDB with a DMB–CN concentration of 250 ppm for 24 hours at 30 °C and pH 7. After incubation, the samples were centrifuged at 1000 rpm and washed with fresh PDB. This process was repeated twice. Finally, the samples were re–suspended in PDB at 1:10 of the original volume.

Human TK6 cells were cultured in 1000 µL of RPMI media with the following DMB–CN concentrations 100, 200, 300 and 400 ppm. The cells were incubated for 24 h at 37 °C in 5% CO_2 and pH 7. After incubation, the samples were centrifuged at 1000 rpm and washed with fresh PBS. This process was repeated twice. Finally, the samples were re–suspended in PBS at 1:10 of the original volume.

The plant cell line *Nicotiana tabacum* was grown in Murashige and Skoog (MS) medium at 20 °C, light 12 h, and 200 rpm for 6 days previous to inoculation with 250 ppm of DMB–CNs. The *N. tabacum* cultures with DMB–CNs were incubated for 24 h at 20 °C, light 12 h, and 200 rpm. After incubation, the samples were centrifuged at 1000 rpm and washed

with fresh MS. This process was repeated twice. Finally, the samples were re–suspended in MS at 1:10 of the original volume.

After re-suspending, the cells were imaged with confocal microscopy using a Zeiss LSM 710 confocal system with Zeiss AXIO Observer Z1 inverted microscope stand with transmitted light (HAL), Illuminator HXP 120C and laser illumination sources. The images were collected under bright field and 405 nm fluorescence excitation. The differences in fluorescence emitted by the DMB–CNs in the cells were determined by image analysis using the software image J.

2.8 Heavy metal ions quenching assays

Stock solutions of the metal ions were prepared at concentrations of 100mM and for DMB–CNs at concentrations of 1000 ppm. All the solutions were prepared using deionised and 0.22 μM filtered water. The metal titration quenching studies utilised DMB–CN solutions of 50 ppm diluted from the 1000 ppm solutions. The fluorescence of the DMB–CN solutions was measured and then the metal solutions were added to the cuvette containing DMB–CNs (50 ppm) to reach a metal concentration of 50 μM. Then, the fluorescence of metal/DMB–CN solution was measured. The reduction in fluorescence was calculated as fluorescence reduction percentage (%) (**Equation 1**).

$$Fluorescence\ reduction\ \% = \left(\frac{FL_0 - FL_{HMt}}{FL_0}\right) \times 100 \qquad \textbf{Equation 1}$$

Where FL_0 is the DMB–CN fluorescence without the addition of heavy metal ions and FL_{HMt} corresponds to the DMB–CN fluorescence after a specific concentration of heavy metal was

added. Metal titration quenching studies were studied, using the heavy metal ion with the highest quenching (Cu (II)) with Cu (II) concentrations from 0.0125 μM up to 50 μM and 50 ppm of DMB–CNs. The range utilised was selected to include the minimum limit for this metal (Cu (II) 1.3 mg/L) and concentrations reported in wastewaters effluents (Zhou et al., 2018).

3 RESULTS

3.1 Biochar depolymerisation

DMB–CNs were produced via a chemical process where DMB was oxidised by the presence of $KMnO_4$ at mild temperatures and pressures. The visual changes in the liquid and solid phase correlated with chemical changes identified using FT–IR spectroscopy. The DMB control and water–treated DMB FT–IR spectra indicated modifications in the biochar chemical groups (**Figure 1a)**. The DMB control and the water–treated DMB had six principal signals 693, 775, 873, the broad band between 1000 and 1100, 1403, and, 1633 cm^{-1}. In contrast, the $KMnO_4$ addition caused changes in the DMB FTIR spectra producing changes in peak position, magnitude and shape. The $KMnO_4$ oxidised DMB had five signals at 917, 1030, 1403, 1633, and 3100–3600 cm^{-1}. The formation of a peak at 917 cm^{-1} was the most significant change in the $KMnO_4$ oxidised DMB. Other changes observed were the decrease of the signals at 873, 1033, and, 1403 cm^{-1}, the disappearance of the 693 cm^{-1} signal, and an increased signal at 1633 cm^{-1}. The significant reduction in the signals at 873 and 1403 cm^{-1} demonstrated a drop in the aromatic carbons in the biochar after the reaction (Gunasekaran et al., 2008; Lou et al., 2015) connected to the release of aromatic structures into the aqueous medium or the opening of aromatic rings. The increased signal at 1633 cm^{-1} is associated with the presence of COO^{-} and C=O linkages correlated with the opening of aromatic rings,

because alcohols and acids resulted from the opening of aromatic rings when they react with $KMnO_4$ (Plácido and Capareda, 2015).

The FT–IR spectrum from $KMnO_4$ control solution (**Figure 1b**), liquid phase from water-treated DMB and liquid phase obtained from the depolymerised DMB. The $KMnO_4$ control solution exhibited characteristic signals at 910 and 1627 cm^{-1}. The depolymerised DMB liquid phase had a brown colour and its FT–IR spectrum had four principal signals at 1010, 1000–1200, 1200–1500, and 1500–1700 cm^{-1}. The most intense bands, 1200–1500 cm^{-1} and 1500–1700 cm^{-1}, were associated with carbon linkages (C–O–C and C–OH bending, C–H bonds, CH_3) C=C bonds, and aromatic structures. The presence of carbon associated peaks in the liquid phase evidenced the releasing of carbonaceous compounds from the DMB during the depolymerisation process. The FT–IR spectrum of water–treated DMB indicated the release of an insignificant amount of compounds to the liquid phase. In summary, the FT–IR spectra demonstrated DMB depolymerisation and the release of carbonaceous compounds into the liquid phase. The released compounds had signals associated with carboxylic acids, hydroxyl groups and aromatic carbons.

3.2 Purification of DMB–derived carbonaceous nanomaterials (DMB–CNs)

The liquid phases after the depolymerisation reaction were purified using three steps of acetone extraction, yielding 10 different fractions labelled sequentially E1 through E10. **Figure 2a** shows the extraction yield of each fraction as a mass percentage. The fractions associated with the initial colloidal suspension reached a summed recovery percentage (E5-E8) of approximately 50 %, with the E8 fraction with the highest recovery percentage. In

contrast, the fractions resulting from the initial supernatant summed a recovery close to 40 %. The highest recoveries were found in the fractions E1 (16 %) and E3 (14 %). In total, the recovery was above 90 % with the material lost during the purification process corresponding to the volumes retired for fraction characterisation.

While all the fractions were fluorescent, the emission and excitation wavelengths, and fluorescence intensity varied. The fluorescence of each raw extraction was measured using four excitation wavelengths 350, 400, 450 and 500 nm. All the fractions (**Figure 2b**), with the exception of fraction E8, exhibited maximum emission when excited at 350 nm. While the maximum emission from these fractions decreased as the excitation wavelength increased, emission was not observed at an excitation wavelength above 500 nm.

The E1-E10 fractions under a 350 nm excitation wavelength had two principal emission wavelengths 420 nm (E1 and E2) and 440 nm (E3-E8 and E10) (**Figure 2b**). Fractions E3 through E8 and E10 (Acetone 3 extraction) originated from a colloidal suspension in either acetone extractions 1 or acetone extraction 2. The Stokes' shifts (difference between maximum emission and excitation wavelengths) in the supernatant fractions E1 and E2 (70 nm) fractions were smaller than that of the colloidal suspension fractions (90 nm).

The fractions were diluted to the same concentration in weight (500 ppm) to determine which fraction had the highest fluorescence yield (**Figure 2c**). The strongest signals were produced by fractions E1 and E8. Fraction E1 produced almost two times more fluorescence than E8, and at least 4 times more than any other fraction. Fraction E8 fluorescence increased

more than 100–fold between the experiment with the complete extracted fraction and the 500 ppm solution.. The E8 emission at a lower concentration, increases. This phenomenon may be associated with self-quenching as the concentration of the initial experiment prevented the emission at 350 nm (**Figure 2a**). The maximum emission wavelength of 420 and 440 nm remained the same as in the initial experiment. As the fraction E1 emission was statistically different ($p<0.05$) from the other fractions (supplementary material), fraction E1 was selected as the most promising fraction for optical applications because of its fluorescence and utilised for further characterisation.

3.3 Dairy manure biochar–derived carbonaceous nanomaterials characterisation

The E1 fraction was characterised spectroscopically and morphologically. **Figure 3** summarises the spectroscopic characterisation. This fraction will be defined as dairy manure biochar–derived carbonaceous nanomaterials E1 fraction (DMB–CN-E1). The FT–IR spectrum (**Figure 3a**) had three bands from 950 to 1050 cm^{-1}, 1100 to 1500 cm^{-1}, and 1500 to 1700 cm^{-1}. The most intense band was the band from 1100 to 1500 cm^{-1}. This band contained the highest peak at 1365 cm^{-1} (C–O–C and C–OH bending) and a lower-shoulder peak around 1305 cm^{-1} (C–H bonds, CH_3). The 1500 to 1700 cm^{-1} band had two peaks, a well–defined peak at 1542 cm^{-1} (C–C skeletal vibrations) and a flat shoulder at 1618 cm^{-1} (C–O vibrations). The 950 to 1050 cm^{-1} was the least intense signal, and was centred at 1010 cm^{-1} (Si–O or with C–O). After evaluating several excitation and emission wavelengths, the emission and excitation spectra (**Figure 3b**) evidenced the strongest emission at 420 nm with an excitation wavelength of 337 nm. The zeta potential of the DMB–CN-E1 was –61.2 mV, indicating strong negatively charged molecules with high stability. A negative zeta potential facilitates interactions with positively charged particles such as heavy metal ions.

Additionally, the DMB–CN-E1 in solution had a hydrodynamic diameter of 110 nm. The UV–Vis spectrum and the sample's electrophoresis gel are included in the supplementary material.

The fluorescence emitted by the DMB–CN-E1 solutions presented a slight, reversible variation when the pH of the solution was modified **(Figure 3a).** From the initial measurements at pH 10, the emission reduced 5 % and 10 % at pH 8 and 6, respectively. Further pH reduction to pH 4 resulted in the DMB–CN-E1 fluorescence reaching values 3 % greater than the original fluorescence at pH 10. As expected, the excitation spectra mirrored changes in the emission spectra with changing pH. The fluorescence intensity changed, and the shape of the curve at pH 4 and 6 differ from the curves at pH 8 and 10. However, the pH changes did not cause a shift either in the maximum emission or maximum excitation wavelengths. The narrow peak at 425 nm corresponds to the emission signal.

The DMB–CN-E1 FT–IR spectra exhibited greater alterations as the pH was changed (**Figure 3b**). The signals observed at pH 10 were 950 to 1050 cm^{-1}, 1100 to 1500 cm^{-1}, and 1500 to 1700 cm^{-1}. This changed as the pH reduced. At pH 8 the signals at 1365 cm^{-1} (C–O–C and C–OH bending), 1547 cm^{-1} (C–C skeletal vibrations) and 1620 cm^{-1} (C–O vibrations) decreased. Moreover, a significant reduction in the 1365 cm^{-1} signal was observed. The main change was the appearance of a new signal at 1100 cm^{-1} referring to C–O–C bonds. At pH 6, there was a considerable change as the single broad band between 1500 and 1700 cm^{-1}, with local maxima at 1620 and 1547 cm^{-1}, separated into two distinct peaks at 1640 and 1554 cm^{-1} (C–C stretching, C=C aromatic stretching). Additionally, the signal at 1365 cm^{-1} decreased significantly (84 %) compared with the initial pH spectra (10) and pH 8

(70 %). In contrast, the signal at 1100 cm^{-1} increased substantially, becoming the strongest signal in the spectra (OH groups). At pH 4, the FT–IR spectrum is similar to that at pH 6 with a slight reduction in the signal at 1100 cm^{-1}.

Figure 3c illustrates the morphological characterisation of the E1 fraction using AFM microscopy. The AFM image yielded a height distribution following a log-normal distribution (**Figure 3d**). The height average was 1.1±0.3 nm with a minimum and maximum value of 0.5 and 2 nm. The particles had a lateral dimension between 11 and 28 nm with an average size of 14±3.5 nm. The AFM section shown as white line in **Figure 3c** and as a line graph the height and distance between particles in **Figure 3e** revealed particles of similar heights as reported by the height distribution.

3.4 Biocompatibility studies

The growth curves of *S. cerevisiae, C. albicans,* and *Y. lipolytica* at three pHs (3, 7 and 10) and five concentrations of DMB–CN-E1 (50, 100, 250, 500 and 1000 ppm) were tested (supplementary material). At the pH values evaluated and concentrations of 100 ppm or below, there was no variation in the yeast growth curves indicating that the DMB–CN-E1 at those concentrations did not affect the growth rate of the yeast studied. At pH 10, the 250 ppm concentration displayed different effects over each yeast. *S. cerevisiae* was completely inhibited, *C. albicans* did not show any inhibition, and *Y. lipolytica* was partially inhibited. At pH 10, 500 and 1000 ppm concentrations completely inhibited growth in the three yeast types. At neutral and acidic pH, there was no indication of inhibited growth at any DMB–CN-E1 concentration. Therefore, inhibition observed at pH 10 with the concentrations

above 100 ppm is most likely associated with a combined effect between DMB–CN-E1 concentration and the pH.

3.5 Cellular Imaging

Figure 4 displays confocal fluorescence microscopy (358 nm excitation wavelength) images recorded after 24 h of growth with the DMB–CN-E1 at pH 7. From the images, the three yeast species seem to interact with the DMB–CN-E1 in different ways. *S. cerevisiae* exhibited a less intense signal than the other yeast. Image analysis showed DMB–CN-E1 fluorescence in *S. cerevisiae* was approximately 6–times lower than that of the other yeast. *C. albicans* and *Y. lipolytica*, had strong fluorescence signals with no statistical difference between the two yeast species. The combined images from the brightfield and fluorescence in *Y. lipolytica* and *C. albicans* provided evidence indicating DMB-CN-E1 trapped within cytoplasmic organelles. In contrast, the DMB–CN-E1 inside *S. cervisiase* seem dispersed throughout the cell cytoplasm. Comparing **Figure 4** images with previously reported yeast fluorescence images, the localisation of DMB–CN-E1 appears to be in the yeast nucleus (Kume et al., 2017) or/and vacuoles (Eide, 2006; Johnston et al., 2013). The control using only PDB did not generate any fluorescence associated with either the DMB–CN-E1 or any autofluorescence from the yeast.

The uptake of DMB–CN-E1 by plant and human cell line was evaluated *in vivo* utilising the strong emission from the DMB–CN-E1under 405 nm excitation. **Figure 5** displays confocal fluorescence microscopy images for TK6 cells and *N. tabacum* after 24 h of culture with 250 ppm of DMB–CN-E1. The TK6 cells showed fluorescence across the entire cell with intense zones and spots observed (**Figure 5a**). It was not possible to identify the

DMB–CN-E1 in a particular location or organelle. The corrected total cell fluorescence analysis evidenced that concentrations 100, 200 and 300 ppm produced a fluorescence significantly different than the control (**Figure 5b**). At 400 ppm, the fluorescence signal seems to drop drastically. This is due to the decrease in the number of the cells for fluorescence quantification. The *N. tabacum* control without DMB–CN-E1 evidenced autofluorescence that spectrally overlapped the DMB–CN-E1 emission. Therefore, the fluorescence observed in the cells corresponded to a mixture between the DMB–CN-E1 fluorescence and *N. tabacum* autofluorescence (**Figure 5c**). The image analysis evidenced a 25 % fluorescence increase in the samples with DMB–CN-E1 compared with the control (**Figure 5d**). This difference was statistically significant, demonstrating that DMB–CN-E1 were present in the plant cells (**Figure 5d**).

The fluorescence of the cells/DMB–CN-E1 was reproducible in different cellular models. In general, the cells uptake DMB–CN-E1 inside cytoplasmic organelles, especially in *Y. lipolytica* and *C. albicans*. TK6 and *S. cerevisiae*, exhibited DMB-CNs distributed throughout the cells instead of located in specific locations/organelles. The capability of DMB-CNs to penetrate different type of cells opens the door for novel methodologies for detection, identification or biosensing of intracellular events in different type of organisms based on these water dispersible and renewably produced DMB–CN.

3.6 Heavy metal ions detection

To evaluate the relevance of DMB–CN-E1 to fluorescence-based metal ion sensing, fluorescence quenching experiments were performed with Cu (II), Co (II), Ni (II), Fe (II), Pb

(II), Hg (II), Ag (I), Mn (II), Li (I), Mo (VI), Ba (II) and Zn (II) (**Figure 6a**). From the twelve metal ions used, eight were able to quench the DMB-CN fluorescence above 15 % (Cu (II), Co (II), Ni (II), Fe (II), Pb (II), Hg (II), Ag (I) and Mn (II)). While, Li (I), Mo (VI), Ba (II) and Zn (II) did not achieved a significant quenching (i.e. < 1 %). The most significant fluorescence reduction was achieved by the Cu (II) (41 %) followed by the Co (II) (31 %) and Ni (II) (30 %). As several heavy metal ions significantly quenched the DMB–CN-E1 fluorescence, this indicated the presence of carboxylic and phenolic groups facilitating the interactions between the DMB–CN-E1 and heavy metal ions. The DMB–CN-E1 capability as a heavy metal sensor was evaluated for Cu (II) detection as it was the ion that achieved the highest quenching. **Figure 6b** depicts the fluorescence spectra of the DMB–CN-E1 after adding different concentration of Cu (II). For this metal the limit of detection was 0.3 μM. The Stern-Volmer plot (**Figure 6b** embedded plot) described the relationship between fluorescence quenching and the metal ion concentration as non-linear with downward curvature. This type of Stern-Volmer curve is characteristics of pure collisional quenching with accessible and inaccessible quenching sites.

4 DISCUSSION

The combination of chemical oxidation and solvent purification produced purified carbonaceous nanomaterials with optical characteristics for imaging applications from dairy manure biochar. Acetone was selected as the solvent because it is miscible and polar, and produces two phases. Additionally, acetone had the advantages of a low boiling point, low cost and facile recovery. After three acetone extractions, 10 different fractions with different levels of fluorescence were produced. The E1 fraction was selected for complete characterisation because its optical properties and recovery yield. The E1 fraction

corresponded to 15 % of the total depolymerised material in the liquid phase. Therefore, the remaining 85 % of the depolymerised materials must still be investigated.

DMB–CN-E1 had similar properties to other carbonaceous nanomaterials produced from cow manure and other types of biomass (**Table 2**). DMB–CN-E1 had maximum emission and excitation wavelengths in the same range as the majority of the Cdots. As with Cdots from other types of biomass, DMB–CN-E1 emission maximum shifts with excitation wavelength (**Figure 3**). The DMB–CN-E1 height and lateral dimensions were larger than the majority of the other carbonaceous nanomaterials' lateral dimensions. Two materials described in literature that had a greater diameter were the Urine-derived Cdots and vitamin C urine-derived Cdots (Essner et al., 2016).

The DMB–CN-E1 were biocompatible with the different species of yeast evaluated. In yeast, the growth curves were affected only at the most alkaline pH and the highest concentrations of 250, 500 and 1000 ppm. This effect on the yeast growth was associated with the increase of the medium pH, which is recognised as a source of inhibition in yeast. Peña et al. (Peña et al., 2015) described *S. cerevisiae* as a more sensitive yeast at pH above 8 (Peña et al., 2015). This report correlates with the higher inhibition observed by *S. cerevisiae* compared with the *C. albicans, and Y. lipolytica* which were able of growing up to pH 9 (Karam El-Din et al., 2012). Besides yeast, Cdots from other sources have been innocuous to other microorganisms such as *Pseudomonas aeruginosa*, *Escherichia coli*, and *Staphylococcus aureus* (Gao et al., 2017; Mehta et al., 2014; Ritenberg et al., 2016).

The confocal fluorescent images of the three yeast species exhibited differences in the location and uptake of the DMB–CN-E1. In yeast, this is the first study showing evidence of

the dependence between yeast species and carbonaceous nanomaterials localisation and uptake. Similar to *S. cerevisiae*, which exhibited considerable less uptake than the other yeast species, other reports have described differences in uptake and location in other cell cultures (Liu et al., 2015). The fluorescent confocal imaging from the TK6 and *N. tabacum* cells demonstrated the potential that DMB-CNs have as a bio-imaging probe. The distribution of DMB–CN-E1 in TK6 is similar to that observed in the cancer cell lines (MCF-7) using Cdots from glucose and cow manure (D'Angelis do ES et al., 2015). *N. tabacum* auto-fluoresced at the same wavelengths as the DMB–CN-E1. However, the carbonaceous nanomaterials were distinguishable when incubated at concentrations of 250 ppm. Further studies with DMB–CN-E1 will include the modification of their surface to increase their specificity and further evaluation of the optical characteristics such as excitation and emission wavelengths and how to control them. The adaptability as a bioimaging probe demonstrated by DMB–CN-E1 is a significant characteristic since the majority of reports using biomass derived carbonaceous nanomaterials as bioimaging probes are only reported in one type of cell or organism (plants, animals or human) (Xue et al., 2018; Zhang et al., 2018; Zheng et al., 2017). DMB–CN-E1 were able to effectively interact and fluoresce with 5 different types of cells.

The evaluation of DMB–CN-E1 as a probe for heavy metal ions in aqueous systems evidenced significant quenching with different heavy metal ions as well as selectivity issues which will need to be addressed before using this carbonaceous nanomaterial as a probe for heavy metal ions. Microalgae biochar-derived carbon dots (MAB-Cdots) were tested as heavy metal ions sensors for Cu (II), Pb (II) and Ni (II) (Plácido et al., 2019). DMB–CN-E1 exhibited higher fluorescence reducing (%) than MAB-Cdots in all cases. This improved performance might be attributed to a size difference as DMB–CN-E1 are smaller than MAB-

Cdots. In both cases, the Stern-Volmer plot evidenced the presence of a downward curve indicating that both materials had a pure collisional quenching with quenching groups less accessible than others. Following published work in the field, DMB–CN-E1 selectivity can be enhanced through a number of different methodologies such as adding phosphorous or nitrogen groups, coupling a secondary set of materials or performing multivariate statistics (Gogoi et al., 2015; Gu et al., 2016; Lippolis et al., 2018; Ye et al., 2017). DMB–CN-E1 structure has C–O, C=O and C-OH linkages and these functional groups form coordination bonds with heavy metal ions which result in fluorescence reduction. The diverse quenching levels and dynamics exhibited by each heavy metal ion are associated with electronic, chemical and vibrational characteristics (Shtepliuk et al., 2017).

The DMB–CN-E1 corresponded to 3 % of the initial DMB, and 9 % of the non-ash portion of the DMB (38 %). Therefore, for each tonne of DMB, it is possible to produce approximately 30 kg of DMB–CN-E1 for imaging, sensing or other applications. In the current market, carbonaceous nanomaterials for imaging such as Cdots and graphene quantum dots are sold for between £129 and £200 for solutions of 10 to 50 mL with a materials concentrations between 1 and 2 mg mL^{-1}. Using a conservative estimation of a market price for a kg of DMB–CN-E1 as 1% of the competitors (1.29 £/kg). Based on retail sales prices, the production and extraction method demonstrated in this article could generate an added-value product with 18-times more value than the original DMB (0.076 £/kg). As the DMB–CN-E1 had similar properties to other Cdots used as fluorescence imaging probes, this technique presents an opportunity for this type of material to participate in the global market for biologic imaging reagents valued at £7.1 billion in 2012 with an expected growth to £9.4 billion by 2017 (BCC Research, 2013). Compared with hydrothermal methods (8–24 h, 180–300 °C) for the production of imaging reagents from biomass (Cdots), chemical

depolymerisation and solvent extraction produced fluorescence probes in half the time (4 h) with similar properties. The processing time reduction has significant repercussions in terms of cost reductions via reduced energy consumption as chemical depolymerisation is faster and occurs at lower temperatures. Future work includes the application of DMB–CN-E1 in other fluorescence sensing applications such as the detection of communicable/non-communicable diseases and organic pollutants, the analysis of the other fractions from the acetone extraction, and the evaluation of bioenergy biochar from other feedstocks as sources for carbonaceous nanomaterials.

5 CONCLUSIONS

Biochar chemical depolymerisation and solvent extraction was proven to be an effective method to produce carbonaceous nanomaterials from dairy manure biochar. The acetone extraction produced 10 fractions and one of them (E1) was selected for further characterisation due to its high fluorescence (DMB–CN-E1). DMB–CN-E1 was characterised spectrophotometrically and morphologically, exhibiting a negative charge, an average lateral dimension of 14 nm and an average height of 1 nm. The DMB–CN-E1 structure was rich in carboxylic and hydroxyl linkages. DMB–CN-E1 was evaluated in different cellular models (yeast, plants and human cells) and exhibited unique localisation patterns dependent in yeast. Furthermore, the DMB–CN-E1 was biocompatible with the cellular models for 24 hours and the doses studied. DMB–CN-E1 had similar properties to previously produced biomass derived carbon dots. DMB–CN-E1 was quenched by heavy metal ions showing their future for heavy metal ions sensing or removal applications. Chemical depolymerisation and solvent extraction produced carbonaceous nanomaterials with similar optical and physical properties compared with methods previously utilised for producing carbonaceous nanomaterials from biomass but in half the processing time and with less energy use. These advantages open the

opportunity for generating added-value nanomaterials (NanoRefinery) from dairy manure biochar gasification, increase the value of biochar for gasification plants and the future application of DMB-CNs as fluorescent probes in commercial bioimaging.

6 ACKNOWLEDGMENTS

The authors would like to thank the financial support provided by the European Regional Development Fund/Welsh Government funded BEACON+ research programme (Swansea University). The Centre for NanoHealth at Swansea University for the support provided by and use of the equipment and installations. Dr Sergio Capareda and his laboratory Bio-Energy Testing and Analysis Laboratory (BETA Lab) at Texas A&M University for supply the samples utilised in this research work.

7 REFERENCES

An J, Yan M, Yang Z, Li T, Zhou Q. A turn-on fluorescent sensor for Zn (II) based on fluorescein-coumarin conjugate. Dyes and Pigments 2013;99:1-5.

Angın D, Köse TE, Selengil U. Production and characterization of activated carbon prepared from safflower seed cake biochar and its ability to absorb reactive dyestuff. Appl Surf Sci 2013;280:705-10. http://dx.doi.org/10.1016/j.apsusc.2013.05.046.

Asyana V, Haryanto F, Fitri L, Ridwan T, Anwary F, Soekersi H. Analysis of urinary stone based on a spectrum absorption FTIR-ATR 2016;694:012051.

BCC Research. **Biologic Imaging Reagents: Technologies and Global Markets** 2013.

Burg V, Bowman G, Haubensak M, Baier U, Thees O. Valorization of an untapped resource: Energy and greenhouse gas emissions benefits of converting manure to biogas through anaerobic digestion. Resour Conserv Recycling 2018;136:53-62.

D'Angelis do ES B, Corrêa JR, Medeiros GA, Barreto G, Magalhães KG, de Oliveira AL et al. Carbon Dots (C‑dots) from Cow Manure with Impressive Subcellular Selectivity Tuned by Simple Chemical Modification. Chemistry-A European Journal 2015;21:5055-60.

Deal C, Brewer CE, Brown RC, Okure MAE, Amoding A. Comparison of kiln-derived and gasifier-derived biochars as soil amendments in the humid tropics. Biomass Bioenergy 2012;37:161-8. http://dx.doi.org/10.1016/j.biombioe.2011.12.017.

Dhenadhayalan N, Lin K. Chemically induced fluorescence switching of carbon-dots and its multiple logic gate implementation. Scientific reports 2015;5:10012.

Eide DJ. Zinc transporters and the cellular trafficking of zinc. Biochimica et Biophysica Acta (BBA)-Molecular Cell Research 2006;1763:711-22.

Essner JB, Laber CH, Ravula S, Polo-Parada L, Baker GA. Pee-dots: biocompatible fluorescent carbon dots derived from the upcycling of urine. Green Chem 2016;18:243-50.

Fan L, Qin J, Li T, Wang B, Yang Z. A novel rhodamine chromone-based "Off–On" chemosensor for the differential detection of Al (III) and Zn (II) in aqueous solutions. Sensors Actuators B: Chem 2014;203:550-6.

Gao Y, Pramanik A, Begum S, Sweet C, Jones S, Alamgir A et al. Multifunctional Biochar for Highly Efficient Capture, Identification, and Removal of Toxic Metals and Superbugs from Water Samples. ACS Omega 2017;2:7730-8.

Genuino DAD, Bataller BG, Capareda SC, de Luna, Mark Daniel G. Application of artificial neural network in the modeling and optimization of humic acid extraction from municipal solid waste biochar. Journal of Environmental Chemical Engineering 2017;5:4101-7.

Gogoi N, Barooah M, Majumdar G, Chowdhury D. Carbon dots rooted agarose hydrogel hybrid platform for optical detection and separation of heavy metal ions. ACS applied materials & interfaces 2015;7:3058-67.

Gu D, Shang S, Yu Q, Shen J. Green synthesis of nitrogen-doped carbon dots from lotus root for Hg (II) ions detection and cell imaging. Appl Surf Sci 2016;390:38-42.

Gunasekaran S, Devi TR, Sakthivel P. Qualitative and Quantitative Analysis on Fibrates-A Spectroscopic Study. Asian Journal of Chemistry 2008;20:4249.

Guo XM, Trably E, Latrille E, Carrère H, Steyer J. Hydrogen production from agricultural waste by dark fermentation: A review. International Journal of Hydrogen Energy 2010;35:10660-73. https://doi.org/10.1016/j.ijhydene.2010.03.008.

Hayati‐Ashtiani M. Characterization of Nano‐Porous Bentonite (Montmorillonite) Particles using FTIR and BET‐BJH Analyses. Particle & Particle Systems Characterization 2011;28:71-6.

Holm-Nielsen JB, Al Seadi T, Oleskowicz-Popiel P. The future of anaerobic digestion and biogas utilization. Bioresour Technol 2009;100:5478-84.

Johnston DA, Tapia AL, Eberle KE, Palmer GE. Three prevacuolar compartment Rab GTPases impact Candida albicans hyphal growth. Eukaryot Cell 2013;12:1039-50. 10.1128/EC.00359-12 [doi].

Karam El-Din AA, Al-Basri HM, El-Naggar MY. Critical factors affecting the adherence of Candida albicans to the vaginal epithelium. Journal of Taibah University for Science 2012;6:10-8. https://doi.org/10.1016/j.jtusci.2012.10.001.

Kume K, Cantwell H, Neumann FR, Jones AW, Snijders AP, Nurse P. A systematic genomic screen implicates nucleocytoplasmic transport and membrane growth in nuclear size control. PLoS genetics 2017;13:e1006767.

Li J, Yin C, Huo F. Development of fluorescent zinc chemosensors based on various fluorophores and their applications in zinc recognition. Dyes and Pigments 2016;131:100-33. https://doi.org/10.1016/j.dyepig.2016.03.043.

Liou Y, Huang W. A Process for Preparing High Graphene Sheet Content Carbon Materials from Biochar Materials 2015.

Lippolis V, Lvova L, Garau A, Giorgi L, Fusi V, Coroleo F et al. A fluorescent sensor array based on heteroatomic macrocyclic fluorophores for the detection of polluting species in natural water samples. Frontiers in chemistry 2018;6:258.

Liu J, Cao L, LeCroy GE, Wang P, Meziani MJ, Dong Y et al. Carbon "quantum" dots for fluorescence labeling of cells. ACS applied materials & interfaces 2015;7:19439-45.

Lou Y, Joseph S, Li L, Graber ER, Liu X, Pan G. Water extract from straw biochar used for plant growth promotion: an initial test. BioResources 2015;11:249-66.

Mehta VN, Jha S, Kailasa SK. One-pot green synthesis of carbon dots by using Saccharum officinarum juice for fluorescent imaging of bacteria (Escherichia coli) and yeast (Saccharomyces cerevisiae) cells. Materials Science and Engineering: C 2014;38:20-7. https://doi.org/10.1016/j.msec.2014.01.038.

Mukome FND, Six J, Parikh SJ. The effects of walnut shell and wood feedstock biochar amendments on greenhouse gas emissions from a fertile soil. Geoderma 2013;200–201:90-8. http://dx.doi.org/10.1016/j.geoderma.2013.02.004.

Nam H, Maglinao AL, Capareda SC. Effective use of dairy manure mixed with sand bedding for gasification. Transactions of the ASABE 2017;60:5-16.

Nam H, Maglinao AL, Capareda SC, Rodriguez-Alejandro DA. Enriched-air fluidized bed gasification using bench and pilot scale reactors of dairy manure with sand bedding based on response surface methods. Energy 2016;95:187-99.

Nguyen HV, Richtera L, Moulick A, Xhaxhiu K, Kudr J, Cernei N et al. Electrochemical sensing of etoposide using carbon quantum dot modified glassy carbon electrode. Analyst 2016;141:2665-75.

Palanivel R, Velraj G. FTIR and FT-Raman spectroscopic studies of fired clay artifacts recently excavated in Tamilnadu, India 2007.

Park J, Hung I, Gan Z, Rojas OJ, Lim KH, Park S. Activated carbon from biochar: Influence of its physicochemical properties on the sorption characteristics of phenanthrene. Bioresour Technol 2013;149:383-9. http://dx.doi.org/10.1016/j.biortech.2013.09.085.

Peña A, Sánchez NS, Álvarez H, Calahorra M, Ramírez J. Effects of high medium pH on growth, metabolism and transport in Saccharomyces cerevisiae. FEMS yeast research 2015;15.

Plácido J, Bustamante-López S, Meissner KE, Kelly DE, Kelly SL. Microalgae biochar-derived carbon dots and their application in heavy metal sensing in aqueous systems. Science of The Total Environment 2019;656:531-9. https://doi.org/10.1016/j.scitotenv.2018.11.393.

Plácido J, Capareda S. Production of silicon compounds and fulvic acids from cotton wastes biochar using chemical depolymerization. Industrial Crops and Products 2015;67:270-80. http://dx.doi.org/10.1016/j.indcrop.2015.01.027.

Ramírez-Arpide FR, Demirer GN, Gallegos-Vázquez C, Hernández-Eugenio G, Santoyo-Cortés VH, Espinosa-Solares T. Life cycle assessment of biogas production through anaerobic co-digestion of nopal cladodes and dairy cow manure. J Clean Prod 2018;172:2313-22.

Ritenberg M, Nandi S, Kolusheva S, Dandela R, Meijler MM, Jelinek R. Imaging Pseudomonas aeruginosa Biofilm Extracellular Polymer Scaffolds with Amphiphilic Carbon Dots. ACS chemical biology 2016;11:1265-70.

Shtepliuk I, Caffrey NM, Iakimov T, Khranovskyy V, Abrikosov IA, Yakimova R. On the interaction of toxic Heavy Metals (Cd, Hg, Pb) with graphene quantum dots and infinite graphene. Scientific reports 2017;7:3934.

Tour JM, Metzger A, Ruquan Y, Mann J. Methods of making graphene quantum dots from various carbon sources 2016;PCT/US2015/059437.

Vasimalai N, Vilas-Boas V, Gallo J, de Fátima Cerqueira M, Menéndez-Miranda M, Costa-Fernández JM et al. Green synthesis of fluorescent carbon dots from spices for in vitro imaging and tumour cell growth inhibition. Beilstein journal of nanotechnology 2018;9:530.

Wang D, Xiang X, Yang X, Wang X, Guo Y, Liu W et al. Fluorescein-based chromo-fluorescent probe for zinc in aqueous solution: Spirolactam ring opened or closed?. Sensors Actuators B: Chem 2014;201:246-54.

Wang Z, Yu J, Zhang X, Li N, Liu B, Li Y et al. Large Scale and Controllable Synthesis of Graphene Quantum Dots from Rice Husk Biomass: A Comprehensive Utilization Strategy. ACS applied materials & interfaces 2015.

Wu W, Yang M, Feng Q, McGrouther K, Wang H, Lu H et al. Chemical characterization of rice straw-derived biochar for soil amendment. Biomass Bioenergy 2012;47:268-76. http://dx.doi.org/10.1016/j.biombioe.2012.09.034.

Xue M, Zhao J, Zhan Z, Zhao S, Lan C, Ye F et al. A dual functionalized natural biomass carbon dot from lychee exocarp for cancer cells targetable near-infrared fluorescence imaging and photodynamic therapy. Nanoscale 2018.

Ye Q, Yan F, Luo Y, Wang Y, Zhou X, Chen L. Formation of N, S-codoped fluorescent carbon dots from biomass and their application for the selective detection of mercury and iron ion. Spectrochimica Acta Part A: Molecular and Biomolecular Spectroscopy 2017;173:854-62.

Zhang X, Wang H, Ma C, Niu N, Chen Z, Liu S et al. Seeking value from biomass materials: preparation of coffee bean shell-derived fluorescent carbon dots via molecular aggregation for antioxidation and bioimaging applications. Materials Chemistry Frontiers 2018.

Zheng Y, Xie G, Zhang X, Chen Z, Cai Y, Yu W et al. Bioimaging Application and Growth-Promoting Behavior of Carbon Dots from Pollen on Hydroponically Cultivated Rome Lettuce. ACS Omega 2017;2:3958-65.

Zhou J, Gao F, Jiao T, Xing R, Zhang L, Zhang Q et al. Selective Cu (II) ion removal from wastewater via surface charged self-assembled polystyrene-Schiff base nanocomposites. Colloids Surf Physicochem Eng Aspects 2018;545:60-7.

Zhu Z, Jiang H, Guo S, Cheng Q, Hu Y, Li C. Dual Tuning of Biomass-Derived Hierarchical Carbon Nanostructures for Supercapacitors: the Role of Balanced Meso/Microporosity and Graphene. Sci Rep 2015;5:15936. 10.1038/srep15936 [doi].

8 FIGURES LIST

Table 1. Fractions obtained after three acetone extractions

Fraction	Acetone Extraction 1	Acetone Extraction 2	Acetone Extraction 3
E1*	Supernatant	Supernatant	Supernatant
E2	Supernatant	Supernatant	Colloidal suspension
E3	Supernatant	Colloidal suspension	Supernatant
E4	Supernatant	Colloidal suspension	Colloidal suspension
E5	Colloidal suspension	Supernatant	Supernatant
E6	Colloidal suspension	Supernatant	Colloidal suspension
E7	Colloidal suspension	Colloidal suspension	Supernatant
E8	Colloidal suspension	Colloidal suspension	Colloidal suspension
E9	Solid pellet	Supernatant	Supernatant
E10	Solid pellet	Supernatant	Colloidal suspension

* Characterised fraction

Table 2. Comparative table of biomass derived carbon dots used as bioimaging probes

Substrate	Production method	Exc/Em (nm)[1]	Diameter(nm)	Cellular imaging
Cow manure biochar	Chemical depolymerisation and solvent extraction 4 h	337/420	14	*S. cerevisiae*, *C. albicans*, *Y. lipolytica*, TK6 cells, *N. tabacum* cells
Pollen	Sonication and hydrothermal 200 °C, 24 h	360/432	5.2	Lettuce roots, leaves and plants
Cow manure	300 °C, 3 h and refluxed in nitric acid for 72 h	365 /450	4	Breast cancer cell (MCF-7)
Cinnamon	Hydrothermal 200 °C, 12 h	370/465	3.4	LN-229 cells, HK-2 cells
Red chilli	Hydrothermal 200 °C, 12 h	380/477	3.1	LN-229 cells, HK-2 cells
Turmeric	Hydrothermal 200 °C, 12 h	370/460	4.3	LN-229 cells, HK-2 cells
Black pepper	Hydrothermal 200 °C, 12 h	390/489	3.5	LN-229 cells, HK-2 cells
Lychee exocarp	Carbonisation	420/520	1.4	Bel-7404 cells
Coffee bean shell	4% aqueous NaOH and acid precipitation	320/380	1-5	HeLa cells
Date kernel	Hydrothermal 200 °C, 8 h	340/430	1–5	MG-63 cells
Urine	Hydrothermal 200 °C, 12 h	325/392	10–30	MEF cells, BT-474 cells
Vitamin C diet Urine	Hydrothermal 200 °C, 12 h	425/500	1–15	MEF cells, BT-474 cells
Asparagus diet Urine	Hydrothermal 200 °C, 12 h	350/427	17–55	MEF cells, BT-474 cells

1 Exc/Em= Maximum excitation and emission wavelengths

HIGHLIGHTS

- Production of added-value nanomaterials (DMB–CNs) from dairy manure biochar
- Selection of the most suitable nanomaterials obtained from dairy manure biochar
- DMB-CNs were used as bioimaging fluorescent probes in different cellular models
- DMB-CNs were used for detecting 12 different heavy metal ions.

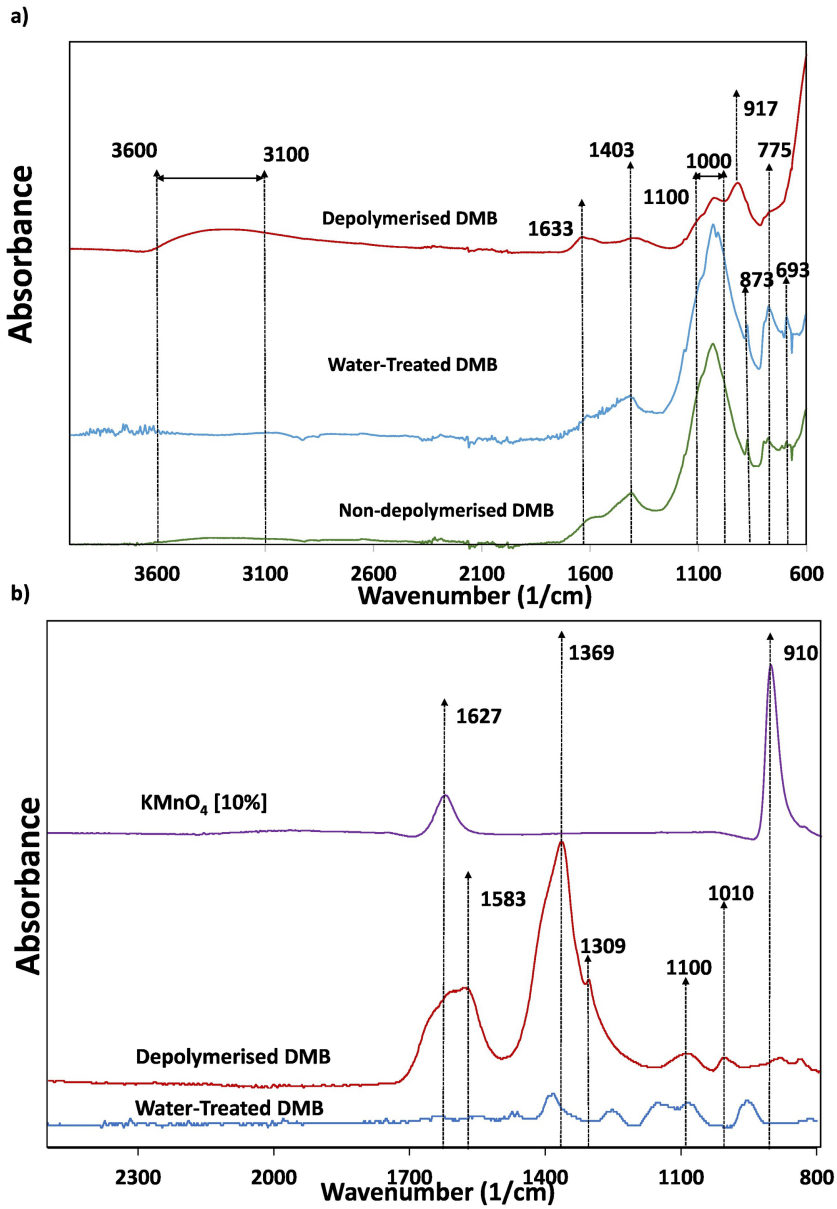
a)
Absorbance
3600
3100
1403
1000
917
775
1100
1633
Depolymerised DMB
873
693
Water-Treated DMB
Non-depolymerised DMB
3600
3100
2600
2100
1600
1100
600
Wavenumber (1/cm)
b)
Absorbance
1369
910
1627
KMnO4 [10%]
1583
1010
1309
1100
Depolymerised DMB
Water-Treated DMB
2300
2000
1700
1400
1100
800
Wavenumber (1/cm)

Figure 1

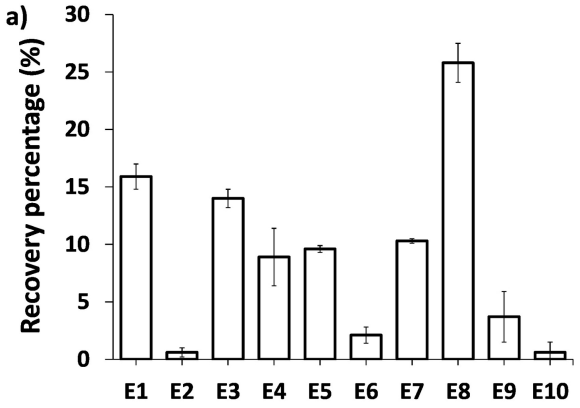
a)
Recovery percentage (%)
30
25
20
15
10
5
0
E1
E2
E3
E4
E5
E6
E7
E8
E9
E10

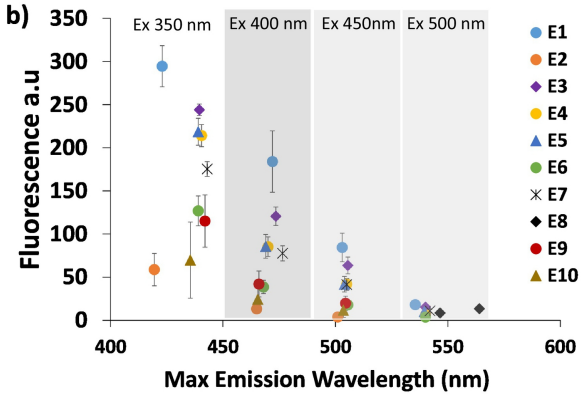
b)
Fluorescence a.u
350
300
250
200
150
100
50
0
Ex 350 nm
Ex 400 nm
Ex 450nm
Ex 500 nm
E1
E2
E3
E4
E5
E6
E7
E8
E9
E10
400
450
500
550
600
Max Emission Wavelength (nm)

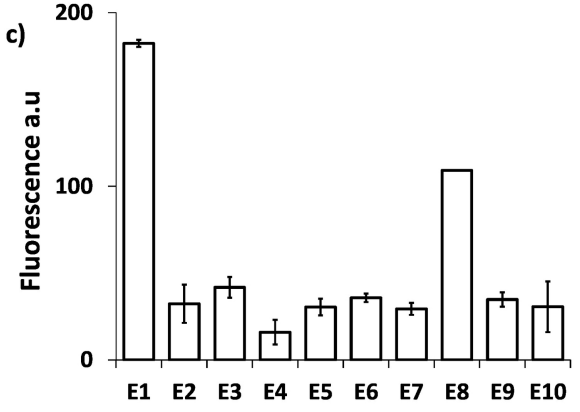
c)
Fluorescence a.u
200
100
0
E1
E2
E3
E4
E5
E6
E7
E8
E9
E10

Figure 2

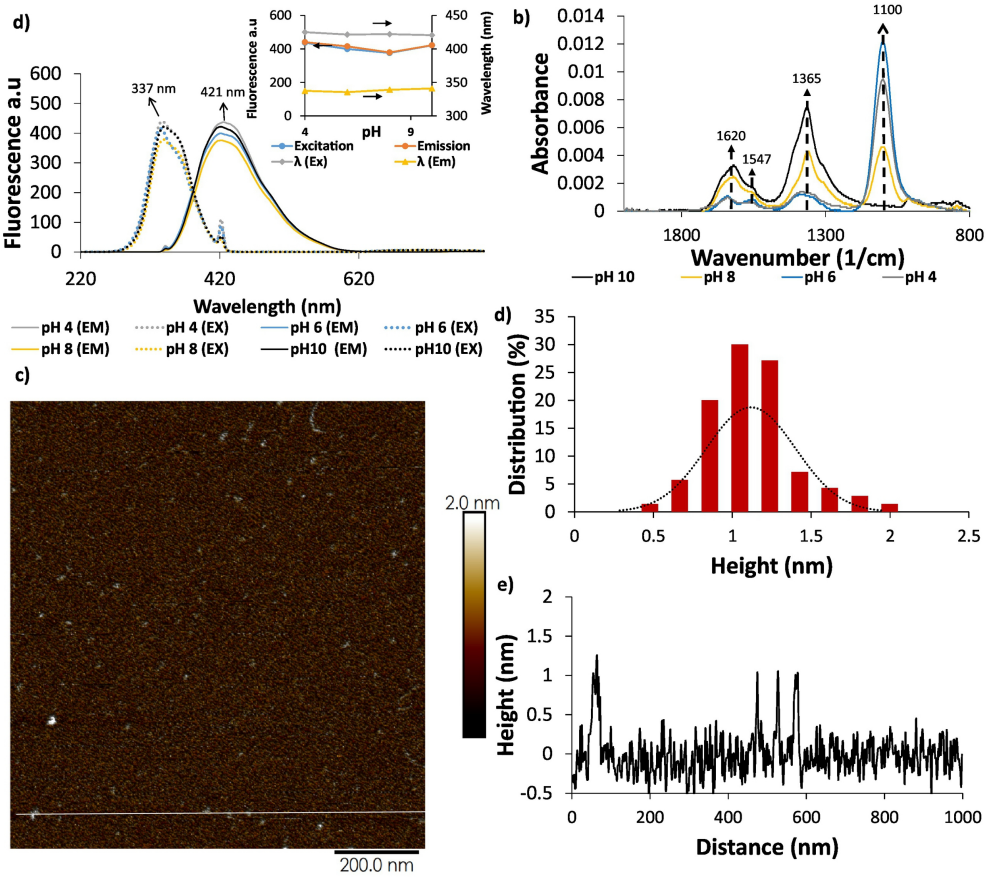
d)
Fluorescence a.u
337 nm
421 nm
Fluorescence a.u
Wavelength (nm)
pH
Excitation
Emission
λ (Ex)
λ (Em)
Wavelength (nm)
pH 4 (EM)
pH 4 (EX)
pH 6 (EM)
pH 6 (EX)
pH 8 (EM)
pH 8 (EX)
pH10 (EM)
pH10 (EX)
b)
Absorbance
1100
1365
1620
1547
Wavenumber (1/cm)
pH 10
pH 8
pH 6
pH 4
c)
2.0 nm
200.0 nm
d)
Distribution (%)
Height (nm)
e)
Height (nm)
Distance (nm)

Figure 3

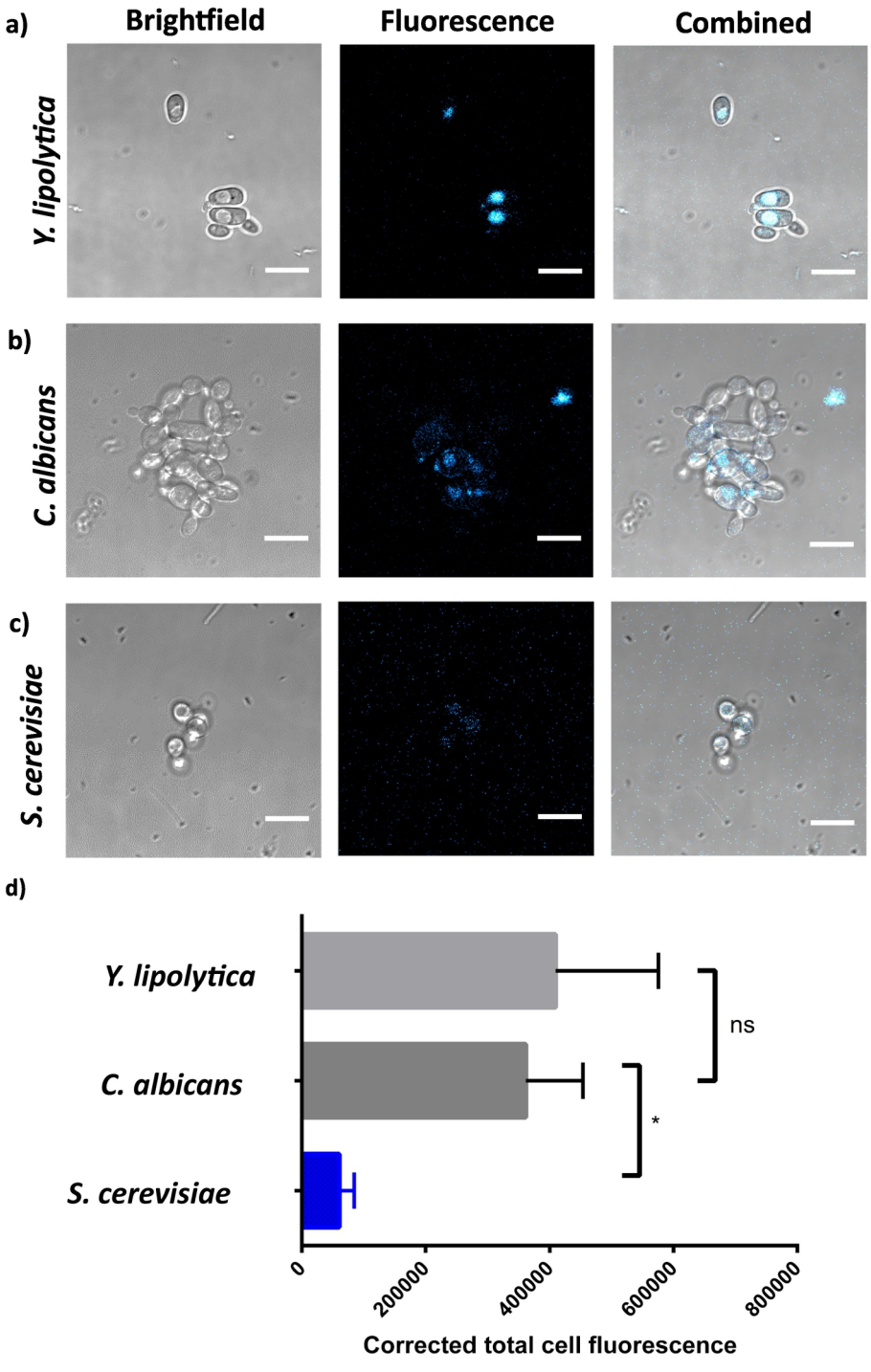
a)
Brightfield
Fluorescence
Combined
Y. lipolytica
b)
C. albicans
c)
S. cerevisiae
d)
Y. lipolytica
C. albicans
S. cerevisiae
ns
*
0
200000
400000
600000
800000
Corrected total cell fluorescence

Figure 4

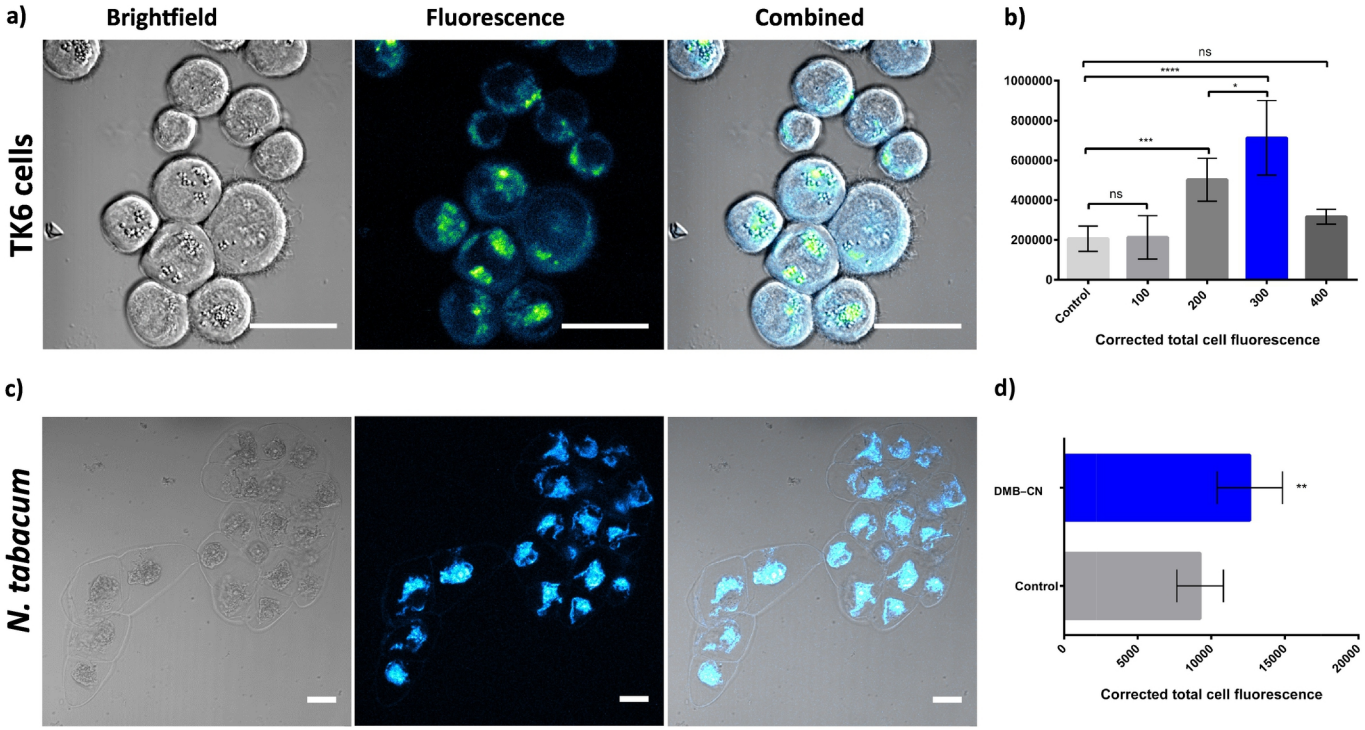
a)
Brightfield
Fluorescence
Combined
TK6 cells
b)
ns
****
*
***
ns
1000000
800000
600000
400000
200000
0
Control
100
200
300
400
Corrected total cell fluorescence
c)
N. tabacum
d)
DMB-CN
Control
**
0
5000
10000
15000
20000
Corrected total cell fluorescence

Figure 5

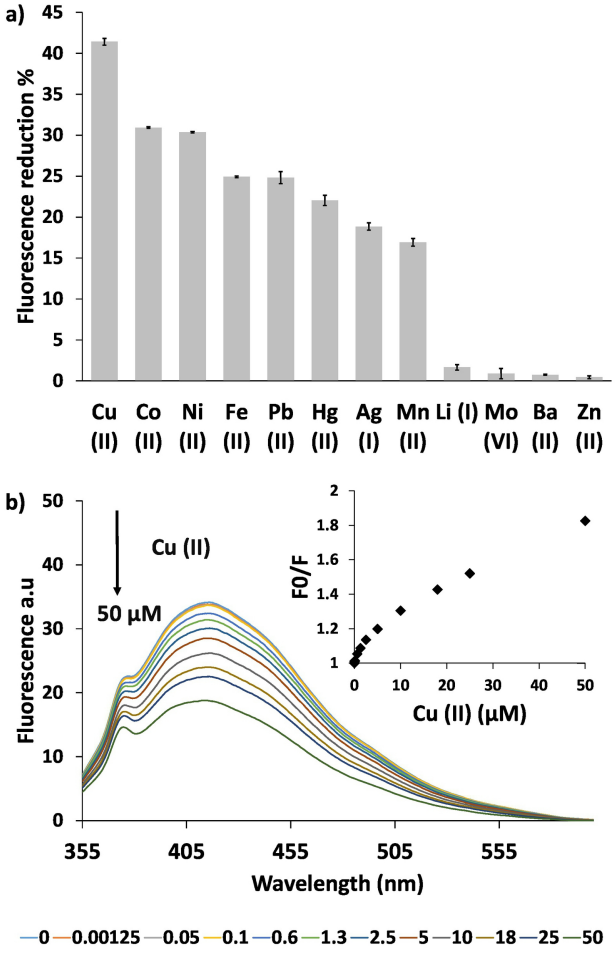
a)
Fluorescence reduction %
45
40
35
30
25
20
15
10
5
0
Cu (II)
Co (II)
Ni (II)
Fe (II)
Pb (II)
Hg (II)
Ag (I)
Mn (II)
Li (I)
Mo (VI)
Ba (II)
Zn (II)
b)
Cu (II)
50 µM
Fluorescence a.u
50
40
30
20
10
0
355
405
455
505
555
Wavelength (nm)
F0/F
2
1.8
1.6
1.4
1.2
1
0
10
20
30
40
50
Cu (II) (µM)
0
0.00125
0.05
0.1
0.6
1.3
2.5
5
10
18
25
50

Figure 6